Ab Initio Study of the Raman Spectra of Amorphous Oxides: Insights into the Boson Peak Nature in Glassy TeO 2

Evgenii Roginskii, Raghvender Raghvender, Olivier Noguera, Philippe Thomas, Olivier Masson, Assil Bouzid

To cite this version:

Evgenii Roginskii, Raghvender Raghvender, Olivier Noguera, Philippe Thomas, Olivier Masson, et al.. Ab Initio Study of the Raman Spectra of Amorphous Oxides: Insights into the Boson Peak Nature in Glassy TeO 2. physica status solidi (RRL) - Rapid Research Letters (pss RRL), 2023, 17 (4), pp.2200505. ⟨10.1002/pssr.202200505⟩. ⟨hal-04267656⟩

HAL Id: hal-04267656

https://hal.science/hal-04267656v1

Submitted on 2 Nov 2023

physica status solidi

Ab initio study of the Raman spectra of amorphous oxides: Insights into the Boson peak nature in glassy TeO_2

E.M. Roginskii*[†], Raghvender Raghvender[‡], Olivier Noguera[‡], Philippe Thomas[‡], Olivier Masson[‡] and Assil Bouzid*[‡]

[†] Ioffe Institute, Polytekhnicheskaya 26, 194021 St. Petersburg, Russia,
[‡] Institut de Recherche sur les Céramiques (IRCER) – UMR CNRS 7315, Université de Limoges, Centre Européen de la Céramique, 12 rue Atlantis, 87068 Limoges Cedex, France

Key words: Raman spectra, DFT, Boson peak, TeO_2, glass

---

* Corresponding author: e.roginskii@mail.ioffe.ru, assil.bouzid@unilim.fr

We present a computational technique that combines density functional theory and the finite difference method to enable the calculation of the Raman spectra of large models of oxide glasses. The calculated Raman spectra of amorphous TeO_2 is found to be in excellent agreement with the experimental data. A strong peak in the low frequency range of the Raman spectra is observed and attributed to the Boson peak. According to atomic-scale analysis, this peak is assigned to collective vibrations of nanoclusters that are formed by the structural units of the glass. Two general factors that influence the Boson peak intensity are established. The first factor concerns the intensity of the low frequency peak in TeO_2 vibrational density of states. The second factor is related to the low frequency vibrational state occupancy at fixed temperature, which obeys the Bose-Einstein statistic. It was found that even a small shift towards high-frequencies leads to a significant decay of the vibrational state occupancy. This correlates quite well when the Raman spectra of TeO_2 glass is compared to the spectra of fused silica. Our technique can be readily applied to the large set of amorphous systems.

Among binary oxide materials, TeO_2 stands out as a peculiar compound in terms of both its structure and its properties. Structurally, TeO_2 occurs in a variety of crystalline polymorphs, including α-TeO_2, β-TeO_2, γ-TeO_2, and δ-TeO_2. When melt-quenched, these crystalline polymorphs lead to glassy TeO_2 that has inherited structural features. In particular, TeO_4 disphenoids with short and long Te-O bonds are the main building blocs of the glass. In addition, the occurrence of Te=O groups is a matter of debate in the community because this would imply that the coordination number of Te (n_{TeO}) is smaller than 4. Recent studies suggest that there is a coordination number reduction and an increase of the short range disorder in the glass as the temperature increases [1,2,3]. On the properties side, TeO_2 features a high refractive index, good non-linear optical properties, high dielectric constant, low phonon energies, high chemical stability, low melting temperatures, large thermo-optical coefficient and wide optical transmittance in the visible to near infrared region [4,5,6,7,8,9]. In particular, its considerably high third-order non-linear susceptibility as compared to the structurally homologous α-SiO_2 [10,11,12,13] makes it useful for a very wide range of applications, such as optical switching devices [14], erasable optical recording media [15], optical amplifiers, up-conversion frequency systems and laser hosts [8,16].

In a recent work, we assessed the effects of the DFT setup and the melt-quench protocol on the equilibrium structure of glassy TeO_2 [17]. The hybrid-functional TeO_2 models that we obtained feature a Te coordination number of 3.96 in the glass and 3.65 in the melt, which is in excellent agreement with recent experimental results. These findings were correlated to the short range disorder in Te- and O-centered structural motifs.

Despite this progress in achieving a good understanding of the structure of glassy TeO_2, research on the vibrational and non-linear optical properties of this glass remains scarce. At a more general level, the computational study of the spectroscopic properties of amorphous systems is limited to the study on atomic clusters that are extracted from the amorphous or crystalline models. While instructive, this procedure is not straightforward and provides an inherently limited understanding of the structural correlations behind the Raman response of the glassy material. From a technical standpoint, the main stumbling block in computing spectroscopic and optical properties is the huge computational effort that is required when dealing with amorphous systems within a periodic DFT calculation. On the one hand, a proper description of these glasses requires an atomistic model that contains several hundreds of atoms. On the other hand, the present methodologies are either suitable for small size systems or only work well in the case of crystalline materials [18,19,20,21,22,23]. Consequently, there is a need for a method that is able to compute accurate Raman properties on large periodic amorphous models at a reasonable computational cost. This method would enable us to access the important quantities that are required to properly correlate the macroscopic properties of the material to its microscopic structure, thereby setting the scene to better design the roots of functional oxide materials.

In this letter, we present a scheme that can compute the Raman spectra of amorphous systems that contain several hundreds of atoms in a periodic simulation cell, which is based on the linear response perturbation theory and the finite differences method. This scheme yields a Raman spectra that is in excellent agreement with the experimental measurements. Furthermore, our scheme allows direct access to the atomistic nature of the normal modes, which facilitates the interpretation of the observed Raman bands, especially in the case of the Boson peak. In this letter, we focus on the Raman properties of amorphous TeO_2 by taking advantage of the achieved atomic scale models in Ref. [17], and we then compare the results to those on amorphous SiO_2. Computational details related to the TeO_2 amorphous model generation protocol can be found in Ref. [17]. The details of the SiO_2 model are provided in the supplementary materials (SI).

At the microscopic level, Raman scattering phenomenon is related to photon-phonon interaction. The result of this inelastic interaction is the change of the energy according to the energy conservation law. In particular, when the photon energy decays after the scattering $\hbar\omega_s = \hbar\omega_i - \hbar\Omega$ (where ω_s and ω_i are the frequencies of the scattered and incipient light, respectively, and Ω is the frequency of the phonon), then this process is called Stokes. When the photon energy increases after scattering, the process is then called Antistokes. The intensity of the Raman scattering depends on the change of the polarizability with respect to atomic displacements which correspond to a selected vibrational mode.

In practice, we start by focusing on the dynamical properties that are computed within the Born-Oppenheimer approximation, which itself is based on the double-harmonic approximation. Given an amorphous configuration, we first optimize the geometry (i.e., variation of the lattice parameters and atomic positions at fixed angles) to achieve a ground state at the minimum of the total energy. Phonon calculations are then performed to extract the vibration frequencies and the normal vectors using the PHONOPY software package [24] to compute the dynamic matrix using the finite difference method.

In a Raman spectrum, the positions of the bands are determined by the vibrational mode frequencies near the Γ-point and in the nonresonant Raman scattering processes. The intensities of the bands can be calculated within a Placzek approximation [25]. For the Stokes process, the intensity of the mth vibrational mode is given by [26]:

$$I^m = \frac{(\omega_0 - \omega_m)^4}{\omega_m} |e_i \cdot A^m \cdot e_s|^2 (n_m + 1), \tag{1}$$

where e_i and e_s are the unit polarization vectors of the incident and scattered radiation, respectively; ω_0 is the frequency of incipient radiation; ω_m is the frequency of the phonon mode; n_m is the Bose-Einstein distribution given by $n(\omega_m) = 1/(e^{\hbar\omega_m/k_B T} - 1)$; and A^m is the Raman tensor, which is defined by:

$$A^m_{ij} = \sqrt{\Omega} \sum_{\alpha,\beta} \frac{\partial \chi_{ij}}{\partial r_{\alpha,\beta}} U^m_{\alpha,\beta}, \tag{2}$$

where Ω is the unitcell volume, $r_{\alpha,\beta}$ is α coordinate of β-th atom in the unitcell, and $U^m_{\alpha,\beta}$ corresponds to normal vector of the m-th vibrational mode. The linear dielectric susceptibility tensor χ_{ij} is obtained within density functional perturbation theory [27] by obtaining the derivative of the macroscopic polarization P with respect to an electric field $\mathcal{E}$:

$$\chi_{ij} = \frac{\partial P_i}{\partial \mathcal{E}_j} = \frac{\partial^2 E_{tot}}{\partial \mathcal{E}_i \partial \mathcal{E}_j} \tag{3}$$

Therefore, the Raman tensor A^m_{ij} is a third order derivative of the total energy with respect to the electric field twice and atomic displacements. While one can use the (2n+1) theorem in quantum mechanics to calculate the third order derivative of the total energy, this technique requires considerable computational effort and implementation of theoretical formalism because one has to access the perturbed wave functions up to the first order. Alternatively, the finite differences method can be applied to calculate the Raman tensor as defined in Eq. (2). This method is based on the generation of structures with atomic displacements along each normal mode in positive and negative directions. This is followed by calculations of susceptibility tensor χ_{ij} for each distorted structure using the linear response approach as implemented in CP2K code [27]. Finally, the values of the Raman tensor components for each vibrational mode are obtained as derivatives of susceptibility with respect to normal vectors obtained by the finite difference methods. Technical details of the implementation of the finite differences method are provided in the supplementary materials.

We note that the following rotational invariants [28] can be used in the case of an amorphous sample:

$$\zeta_i = \frac{1}{3}\left(\alpha^i_{xx} + \alpha^i_{yy} + \alpha^i_{zz}\right), \tag{4}$$

$$\begin{aligned}\gamma_i^2 = \tfrac{1}{2}\left[(\alpha^i_{xx} - \alpha^i_{yy})^2 + (\alpha^i_{yy} - \alpha^i_{zz})^2 + (\alpha^i_{xx} - \alpha^i_{zz})^2\right] + \\ + \tfrac{3}{4}\left[(\alpha^i_{xy} + \alpha^i_{yx})^2 + (\alpha^i_{xz} + \alpha^i_{zx})^2 + (\alpha^i_{yz} + \alpha^i_{zy})^2\right],\end{aligned} \tag{5}$$

Consequently, the intensity of the Raman bands for parallel and crossed polarization can be written as:

$$I_i^{\perp} = \frac{(\omega_L - \omega_i)^4}{\omega_i}\left[n(\omega_i) + 1\right]\frac{\gamma_i^2}{15}, \tag{6}$$

$$I_i^{\parallel} = \frac{(\omega_L - \omega_i)^4}{\omega_i}\left[n(\omega_i) + 1\right]\frac{45\zeta_i^2 + 4\gamma_i^2}{45}. \tag{7}$$

The total Raman activity of powders (i.e., the case of unpolarized scattering) is a sum of both invariants $I_i^{tot} = I_i^{\parallel} + I_i^{\perp}$. Finally, the Raman intensity is calculated according to Eq. (6) and (7), where each peak of the simulated spectra is obtained as a sum of Lorentzian shape lines constructed using the Raman activity of each vibrational mode with a fixed halfwidth. The codes and workflows that are used to achieve these calculations are available at [29].

Following this procedure, we calculated the Raman spectra on glassy TeO_2 and glassy SiO_2 as an average of 10 spectra computed on 10 amorphous configurations that were sampled from the T=300K trajectory of the glass for each system. The results are presented in Fig.1 and are compared to experimental results.

By inspecting the experimental Raman spectra of TeO_2 glass, one can identify several ranges with particular signatures that have been correlated in the literature to particular vibrational modes. In the low wavenumbers region, one can associate the main peak centered around 30 cm^{-1} with the Boson peak [33], while the shoulder around 140 cm^{-1} can be attributed to the intra-chain vibrations of Te-Te bonds [34]. In the central wavenumbers range, a broad peak coincides with the typical signatures of symmetric stretching vibrations in nearly symmetric (425 cm^{-1}) and asymmetric (500 cm^{-1}) Te-O-Te bridges [35,36]. The asymmetric stretching vibrations in nearly symmetric and asymmetric Te-O-Te bridges lead to typical signatures around 605 cm^{-1} and 660 cm^{-1}, respectively [35,36]. Finally, the highest frequency band in the high wavenumber region can be attributed to the asymmetric stretching vibrations in asymmetric Te-O-Te bridges (710 cm^{-1}) and asymmetric stretching of essentially covalent $Te_{eq}O$ bonds (770 cm^{-1}) [35,36].

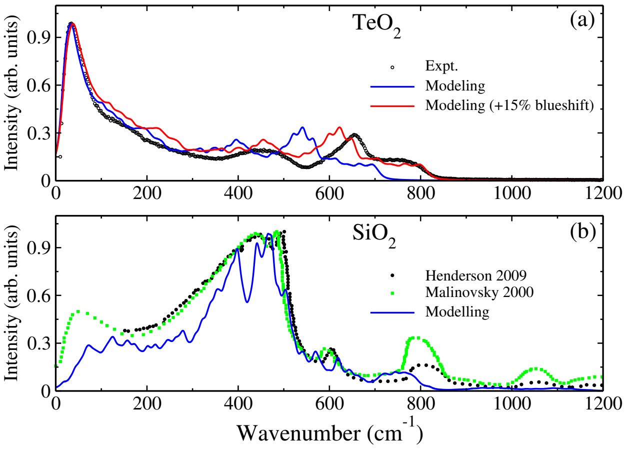

Figure 1 Calculated Raman spectra on glassy TeO_2 (a) and glassy SiO_2 (b) compared to experimental results from Refs. [30], [31], and [32], respectively. A 15% blue shift was applied to the Raman shift in the case of TeO_2. The Raman intensity is normalized to the maximum band intensity.

By following the calculated Raman spectrum (see Fig. 1), one can distinguish all of the observed features in the experimental spectra. Nevertheless, for wavenumbers higher than 300 cm^{-1}, all of the positions of the bands are underestimated by about 15%. This discrepancy is due to the small overestimation of the Te-O bond length in our models by about 0.04 Å [17]. This is a well-known issue and is related to the generalized gradient approximation family of exchange and correlation functionals, which slightly underestimate the lattice parameters and interatomic bond lengths. In addition, the large asymmetry around O atoms might influence the values of the calculated phonon frequencies [17]. Therefore, applying a 15% blueshift leads to modeled spectra that have an unprecedented good agreement with the measured spectra over the whole range of frequencies (see Fig. 1).

Similarly, the calculated Raman spectrum of glassy SiO_2 shows a good reproduction of the experimental spectrum. In this case, we note that there is a very limited blueshift thanks to the very well-defined structure of SiO_2. Compared to TeO_2, the Raman spectrum of glassy SiO_2 features a small peak at around 50 cm^{-1} that corresponds to the Boson peak. Given that the origins of the Boson peak in amorphous TeO_2 remain largely unknown, a comparative study of the Raman spectra between the TeO_2 and SiO_2 can be instructive.

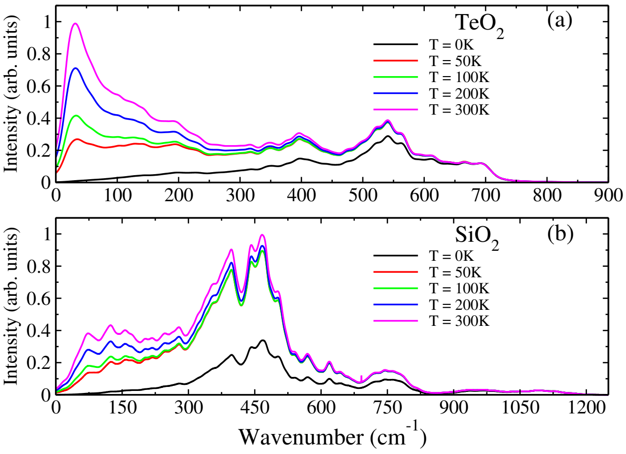

Figure 2 Simulated Raman spectra of glassy TeO_2 (a) and glassy SiO_2 (b) at different temperatures. The spectra are normalized to the highest frequency band, where the effect of pre-factor is minimal.

The Raman intensity of each band calculated using Equation (1) contains two main contributions, the squared Raman tensor components and the pre-factor $\mathcal{G}_m = (1 + n(\omega_m))/\omega_m$, which contains a damping inverse frequency term $1/\omega_m$ multiplied by the Bose-Einstein distribution function $n(\omega_m)$. To disentangle the contributions of the various terms in Equation (1) to the total Raman intensity, in Fig. 2 we show the calculated temperature dependent Raman spectra of TeO_2 and SiO_2. The temperature dependence of the spectra is triggered by the temperature dependence of the Bose-Einstein distribution function $n(\omega_m)$.

It is noteworthy that the simulated Raman spectra at zero temperature reveals no Boson peak feature for both oxides. At zero temperature, the Bose-Einstein term is negated and the pre-factor $\mathcal{G}$ simply acts as a damping function $(1/\omega)$ for the squared Raman tensor components. Interestingly, we observe that the "natural" Raman activity (i.e., squared Raman tensor components) is very small in the low frequency range (the highest intensity band in range [0–50] cm^{-1} is related to the highest intensity band in the whole spectra by 1:100). As temperature increases, the impact of the Bose-Einstein distribution function becomes stronger and one can find a significant response in the Raman spectra in the low frequency range. At T=100 K, one can clearly see that the Bose-Einstein distribution overpowers the damping function in the low frequency range, which leads to an "amplification" of the Raman spectra in the low frequency range (or, in other words, damping intensity and higher frequencies). Therefore, the pre-factor $\mathcal{G}$ takes a key role in the low frequency range Raman spectra. In general, at finite temperature, it acts as an amplifier for low frequency range. The strength of this amplification depends on a competition between the two terms in the pre-factor $\mathcal{G}$ according to the temperature and the frequency of the considered Raman band.

When the nature of the low frequency Raman spectra amplification is established, it is worth comparing the spectra of TeO_2 and SiO_2. At zero temperature, the Raman spectra of TeO_2 shows a steady growth of the intensity, starting rapidly from zero frequency. Actually, the lowest Raman-active vibration is found at 17 cm^{-1}. In the case of SiO_2, the spectra shows a zero intensity at very low frequencies and only starts to grow weakly at approximately 50 cm^{-1} (the lowest frequency Raman-active vibration is found at 32 cm^{-1}). At finite temperature, the band at low frequencies is clearly observed in the case of TeO_2. Nevertheless, in the case of SiO_2 glass, even at T=300 K this band is not as strong as in the Raman spectra of TeO_2. This can be explained by a frequency dependence of the pre-factor $\mathcal{G}$. This dependence follows a simple rule: the amplification of the Raman spectra is higher when the frequency of the band is lower. As mentioned earlier, the smallest phonon frequency of TeO_2 is found at 17 cm^{-1}, while the lowest frequency phonon in the case of silica glass is found at 32 cm^{-1}. This difference in ca. 15 cm^{-1} leads, in part, to a significant difference in the intensity of the Boson peak.

The advantage of the method that is presented in this letter is that it allows us to make a detailed analysis of the Raman bands because it gives access to the normal modes (atomic displacements of vibrational modes) of the Raman active vibrations. By analysing the structural fragments that are involved in vibrations related to the Boson peak, one infers that these modes are the result of collective vibrations of nanoclusters composed by structural units (TeO_4, TeO_3, TeO_5) as a whole. This result is consolidated by investigating the overall weight (impact) of the chemical species (Te and O) in a given Raman active mode, which is calculated as a ratio of the summary displacements made by atoms of a given chemical species with respect to the sum of displacements of all of the atoms in a given vibrational mode. In Figure S3, the weight for each chemical species is plotted as a function of the Raman frequency. It is noteworthy that the weight of O atoms will always be at least twice as much than the weight of the Te atoms because there are twice as many O atoms as Te atoms in TeO_2 glass. This weight proportionality holds true at the low frequency range, where the impact of Te and O atoms is nearly the same (taking a factor of 2 into account). In contrast, the weight of the oxygen atoms becomes dominant in the high frequency range, which indicates the key role of O vibrations in this range of frequencies. The low frequency vibration can be visualized thanks to the obtained eigenvectors of the dynamic matrix. An example of structural unit vibrations is plotted in Figure S4 in the supplementary materials. Understanding the nature of the frequency vibrations provides an explanation of the origin of the weak "natural" Raman activity that is observed at low frequency vibrational modes. The vibrations of structural units as a whole lead to a weak change of the polarizability of the whole system, and therefore to a small Raman response, which in turn is proportional to the derivative of the polarizability with respect to atomic displacements. However, the dominant Te-O vibrations in the middle and high frequency range, including bending, libration and stretching, leads to a significant impact on the polarizibility changes, and consequently to a high Raman activity, which is damped by prefactor $\mathcal{G}$, as discussed earlier.

Finally, the origins of the strong Boson peak in TeO_2, which were explained earlier by the low frequency vibrational states, compared to SiO_2 can be also attributed to the physical properties of both systems. In particular, assuming that the low frequency states are related to displacements of the whole structural units, one can put forward a correlation between their low frequency and the mass of the structural units involved in these vibrational states. In a simple harmonic approximation, the frequency is proportional to the inverse square root of the mass as $\omega = \sqrt{k/m}$. Considering as a first approximation that ω is mostly affected by the mass of the structural units, and bearing in mind that the mass of the structural unit TeO_4 is almost twice that of SiO_4, one can easily establish that the ratio of Boson peak frequency for TeO_4 and SiO_4 systems is equal to $\sqrt{2}$. The experimental frequency of Boson peak of TeO_2 is 35 cm^{-1}. By taking the ratio $\sqrt{2}$ into account, one obtains a frequency shift up to 49.5 cm^{-1} for SiO_2 amorphous silica. This is very close to the experimental data plotted in Figure 1b (see Table S1 in the SI for more details). This correlation is of a particular interest because it is only related to the mass of the structural units involved in the vibrational modes. Therefore, it is possible to predict the approximated position and the strength of the Boson peak in Raman spectra in other amorphous materials.

The Boson peak that is observed in the Raman spectra of amorphous TeO_2 (see Fig.1) is significantly stronger than that in SiO_2. This can be explained, in part, by the high concentration of phonon states in the low-frequency range. The density of phonon states (VDOS) is plotted in Fig. 3. The strong low frequency band in the VDOS of TeO_2, when compared to the much weaker band in the VDOS of SiO_2, rises rapidly and reaches a maximum at frequency $\sim$50 cm^{-1}. In contrast, the low frequency band in VDOS of SiO_2 is very broad and has a maximum at $\sim$130^{-1}. It is noteworthy that the prefactor $\mathcal{G}$ acts as a damping factor at higher frequencies and, in addition to the lower density of states in the VDOS of SiO_2, this is the reason why the Boson peak in the Raman spectra of SiO_2 is weaker than that of TeO_2. These findings show that the intensity and the frequency of the Boson peak can be qualitatively estimated by VDOS analysis.

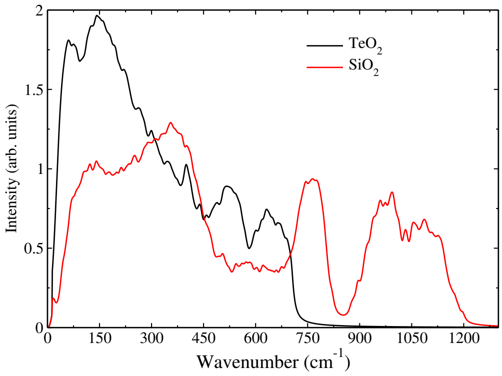

Figure 3 Calculated phonon density of states of amorphous TeO_2 and SiO_2.

The Boson peak is widely interpreted as a consequence of the absence of long-range order and the frequency of the peak maximum is related to a *medium-range order-size* [31], which remains not very well defined. Indeed, an amorphous system can be considered as a crystal system with breaking of the periodic boundary conditions, which leads to many times Brillouin zone (BZ) folding. A good example to explain the appearance of low frequency peaks in Raman spectra due to BZ folding can be found in supercells [37]. Many times BZ folding leads to a complete disorder, which is accompanied by a degeneracy of whole BZ at the Γ point. In the case of ordered structures, the frequency of acoustic vibrations near the Γ-point of the BZ is zero and starts to grow when k-vector shifts along the BZ boundary. The calculated phonon dispersion branches of the γ-TeO_2 crystal accompanied with VDOS compared to those of crystobalite α-SiO_2 are plotted in Figure S5 (see SI). One can find a sharp and strong peak in the VDOS of γ-TeO_2 at a frequency of $\sim$55 cm^{-1}, which is close to the Boson peak frequency in the experimental Raman spectrum. This band mostly consists of acoustic branches, which have a small dispersion due to low sound velocity in TeO_2. In contrast, in the case of α-SiO_2, the low frequency peak in VDOS is weak and broad in the low-frequency range, and has a maximum at $\sim$75 cm^{-1}. The acoustical phonon branches dispersion in α-SiO_2 is higher, and therefore the low frequency band in VDOS consists of a mixture of acoustical and optical phonon branches. This mixture triggers the formation of broad band from 0 up to 500 cm^{-1} with local maxima. The results of crystalline systems VDOS analysis are in line with those made on amorphous systems. Therefore, they can be used for qualitative analysis of the Boson peak nature. In addition, the dispersion of acoustic branches, which is related to sound velocity, is a key feature to predict the strength and position of the Boson peak. Our microscopic approach has shown that the Boson peak corresponds to collective displacements of small size nanoclusters composed from the glassy structural building blocs (e.g., TeO_4). Therefore, one can consider the mean Te-Te (Si-Si) distance as a Boson peak characteristic. In the case of TeO_2, this distance corresponds to the mean shortest Te-Te (Si-Si) distance obtained in Te-

O-Te bridges, which is about 3.75 Å [15]. In the case of SiO_2 glass, the corresponding distance is equal to $\sim$3 Å (see Table S2 in the SI for more details). The minimum distance is responsible for the force constant k value in the simple harmonic approximation, namely the force constant is harder when the distance is shorter. This regularity explains why the Boson peak in case of silica has a higher frequency.

In summary, we present an efficient scheme to calculate the Raman spectra on amorphous periodic glassy oxide models containing several hundreds of atoms by combining the density functional theory and the finite differences method. Our scheme has the advantage of a quite reasonable and time efficient computational cost thanks to the efficient scalability of the CP2K code. The obtained Raman spectra in the case of TeO_2 and SiO_2 demonstrate a high level of agreement with the experiments. In addition, we study the origins of the Boson peak observed in glassy TeO_2 by focusing on two aspects. First, we investigate the reasons behind the strong Boson peak observed in glassy TeO_2 in close comparison to the less pronounced Boson peak reported in glassy SiO_2. We show that the strength and position of the Boson peak is a function of the phonon density of the state's maximum (frequency and intensity). Furthermore, we find that as the frequency increases, the Boson peak is damped by inverse frequency and the Bose-Einstein distribution terms. Consequently, because the TeO_2 shows a lower frequency of the Boson band, it undergoes a higher amplification of its Raman spectra in the low frequency range. Second, we inspect the atomistic nature of the Boson peak by analysing the normal modes vectors and attribute the Boson peak to vibrations of Te-centered structural units as a whole. This leads to characterization of Boson peak by defining a *medium-range ordersize* that is equal to the first maximum in the partial cation-cation pair distribution function in oxide materials, which is very probably the case for the big family of binary (ternary) systems. Overall, we demonstrate that our computational scheme is able to compute accurate Raman spectra of large glassy systems, which paves the way towards a systematic computational study of the vibrational properties of oxide glasses.

Acknowledgements This work was supported by the ANR via the projects TRAFIC (ANR-18-CE08-0016-01) and AMSES (ANR-20-CE08-0021) and by région Nouvelle Aquitaine via the F2MH project AAP NA 2019-1R1M01. This work was also supported by institutional grants from the French National Research Agency under the Investments for the future program with the reference ANR-10-LABX-0074-01 Sigma-LIM. Calculations were performed by using resources from Grand Equipement National de Calcul Intensif (GENCI, grants No. A0080910832, A0080910832, A0100910832 and A0120910832). We are grateful to TGCC for the generous cpu allocation within the special session project spe00019. We used computational resources provided by the computing facilities Mésocentre de Calcul Intensif Aquitain (MCIA) of the Université de Bordeaux and of the Université de Pau et des Pays de l'Adour.

References

[1] E. R. Barney, A. C. Hannon, D. Holland, N. Umesaki, M. Tatsumisago, R. G. Orman, and S. Feller, J. Phys. Chem. Lett. **4**(14), 2312–2316 (2013).

[2] O. Alderman, C. J. Benmore, S. Feller, E. Kamitsos, E. Simandiras, D. G. Liakos, M. Jesuit, M. Boyd, M. Packard, and R. Weber, J. Phys. Chem. Lett. **11**(2), 427–431 (2019).

[3] A. Gulenko, O. Masson, A. Berghout, D. Hamani, and P. Thomas, Phys. Chem. Chem. Phys. **16**(27), 14150–14160 (2014).

[4] J. Stanworth et al., J. Soc. Glass Technol. **38**, 425–435T (1954).

[5] H. Bürger, W. Vogel, and V. Kozhukharov, Infrared Phys. **25**(1), 395–409 (1985).

[6] M. Weber, J. Non-Cryst. Solids **123**(1), 208–222 (1990), XVth International Congress on Glass.

[7] E. Vogel, M. Weber, and D. Krol, Phys. Chem. Glas. **32**(6), 231–254 (1991), cited By 398.

[8] R. A. H. El-Mallawany, Tellurite Glasses Handbook : Physical Properties and Data, Second Edition (CRC Press, April 2016).

[9] T. Honma, N. Ito, T. Komatsu, and V. Dimitrov, J. Am. Ceram. Soc. **93**(10), 3223–3229.

[10] M. Dutreilh-Colas, P. Thomas, J. C. Champarnaud-Mesjard, and E. Fargin, Physics and Chemistry of Glasses - European Journal of Glass Science and Technology Part B **44**(5), 349–352 (2003).

[11] J. R. Duclère, T. Hayakawa, E. Roginskii, M. Smirnov, A. Mirgorodsky, V. Couderc, O. Masson, M. Colas, O. Noguera, V. Rodriguez et al., Journal of Applied Physics **123**(18), 183105 (2018).

[12] E. M. Roginskii, V. G. Kuznetsov, M. B. Smirnov, O. Noguera, J. R. Duclre, M. Colas, O. Masson, and P. Thomas, J. Phys. Chem. C **121**(22), 12365–12374 (2017).

[13] S. H. Kim, T. Yoko, and S. Sakka, Journal of the American Ceramic Society **76**(10), 2486–2490 (1993).

[14] H. Nasu, O. Matsushita, K. Kamiya, H. Kobayashi, and K. Kubodera, J. Non-Cryst. Solids **124**, 275–277 (1990).

[15] K. Kimura, Jpn. J. Appl. Phys. **28**(5R), 810 (1989).

[16] S. Tanabe, K. Hirao, and N. Soga, J. Non-Cryst. Solids **122**(1), 79–82 (1990).

[17] R. Raghvender, A. Bouzid, S. Cadars, D. Hamani, P. Thomas, and O. Masson, Phys. Rev. B **106**(17), 174201 (2022).

[18] P. Partovi-Azar, T. D. Kühne, and P. Kaghazchi, Physical Chemistry Chemical Physics **17**(34), 22009–22014 (2015).

[19] S. Luber, M. Iannuzzi, and J. Hutter, The Journal of Chemical Physics **141**(9), 094503 (2014).

[20] P. Partovi-Azar and T. D. Kühne, Journal of Computational Chemistry **36**(29), 2188–2192 (2015).

[21] A. Calzolari and M. B. Nardelli, Scientific reports **3**(1), 1–6 (2013).

[22] Q. Liang, S. Dwaraknath, and K. A. Persson, Scientific data **6**(1), 1–7 (2019).

[23] M. Lazzeri and F. Mauri, Physical Review Letters **90**(3), 036401 (2003).

[24] A. Togo and I. Tanaka, Scr. Mater. **108**(Nov), 1–5 (2015).

[25] M. Born and R. Huang, Dynamical Theory of Crystal lattices (Oxford University Press, 1954).

[26] M. Cardona and G. Güntherodt (eds.), Light scattering in solids II (Springer-Verlag, Berlin, 1982).

[27] I. Souza, J. Íñiguez, and D. Vanderbilt, Physical Review Letters **89**(11) (2002).

[28] D. A. Long, The Raman effect: A unified treatment of the theory of Raman scattering by molecules (WILEY, 2002).

[29] Raman codes and workflows are available at:, `https://github.com/ladyteam/ramanpy`.

[30] M. R. Zaki, D. Hamani, M. Dutreilh-Colas, J. R. Duclère, O. Masson, and P. Thomas, Journal of Non-Crystalline Solids **484**, 139–148 (2018).

[31] V. Malinovsky, V. Novikov, N. Surovtsev, and A. Shebanin, Physics of the solid state **42**(1), 65–71 (2000).

[32] G. S. Henderson, D. R. Neuville, B. Cochain, and L. Cormier, Journal of Non-Crystalline Solids **355**(8), 468–474 (2009).

[33] A. Sokolov, A. Kisliuk, M. Soltwisch, and D. Quitmann, Physical Review Letters **69**(10), 1540 (1992).

[34] T. Vasileiadis and S. N. Yannopoulos, Journal of Applied Physics **116**(10), 103510 (2014).

[35] J. Champarnaud-Mesjard, S. Blanchandin, P. Thomas, A. Mirgorodsky, T. Merle-Mejean, and B. Frit, Journal of physics and chemistry of solids **61**(9), 1499–1507 (2000).

[36] A. Mirgorodsky, T. Merle-Méjean, J. C. Champarnaud, P. Thomas, and B. Frit, Journal of physics and chemistry of solids **61**(4), 501–509 (2000).

[37] V. Davydov, E. Roginskii, Y. Kitaev, A. Smirnov, I. Eliseyev, D. Nechaev, V. Jmerik, and M. Smirnov, Nanomaterials **11**(2), 286 (2021).

Graphical Table of Contents

GTOC image:

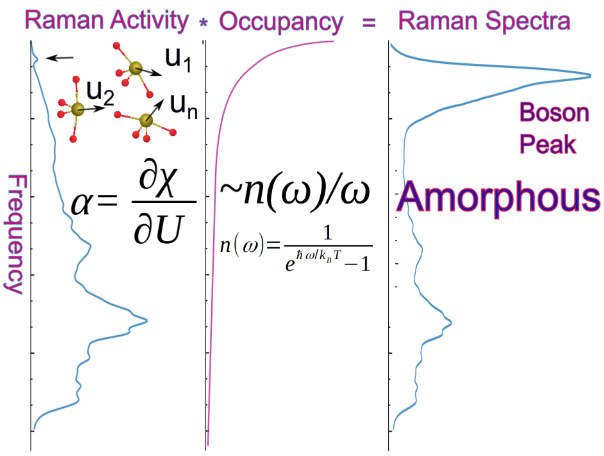

Supporting Information

Ab initio study of the Raman spectra of amorphous oxides: Insights into the Boson peak nature in glassy TeO_2

Evgenii M. Roginskii,[*,†] Raghvender Raghvender,[‡] Olivier Noguera,[‡] Philippe Thomas,[‡] Olivier Masson,[‡] and Assil Bouzid[*,‡]

†*Ioffe Institute, Polytekhnicheskaya 26, 194021 St. Petersburg, Russia*

‡*Institut de Recherche sur les Céramiques (IRCER) – UMR CNRS 7315, Université de Limoges, Centre Européen de la Céramique, 12 rue Atlantis, 87068 Limoges Cedex, France*

E-mail: e.roginskii@mail.ioffe.ru; assil.bouzid@unilim.fr

DFT setup

The DFT calculations presented in this work, were carried out within generalized gradient approximation to density functional theory (DFT) as implemented in CP2K software package.[1] The Perdew-Burke-Ernzerhof (PBE)[2] functional was used in all the calculations. The Gaussian Plane Waves method[3] was used to form wavefunctions basis set with cutoff energy equal to $E_g = 1000$ Ry for planewave part and using triple-zeta valence basis for local combination of molecular orbitals part. Goedecker-Teter-Hutter pseudopotentials are used to describe core-valence interactions.[4] The self consistent calculations were performed with electronic convergence criteria of 10^{-8} Ha. Geometry optimization is performed by relaxing both cell parameters and atomic positions at fixed angles for a given atomistic configuration. During the relaxation, atomic displacements and lattice parameters were varied until forces on atoms become below 10^{-5} Ha/Bohr and pressure below 10^{-2} GPa. Dynamical properties of relaxed structures were carried out using finite difference method.

SiO_2 Models

We have performed *ab-initio* MD to obtained a structural model of SiO_2 glass with 270 atoms at a constant density of 2.2 gm/cm^3. The starting *ab-initio* model was produced after a classical MD run at T = 2000 K for 1000 ps using BKS type potential with potential parameters taken from Ref.[5] Further, the model was quenched to room temperature following the thermal cycle shown in figure [S1] under NVT conditions. The partial pair distribution functions (PDFs) of the glass are shown in figure [S2]).

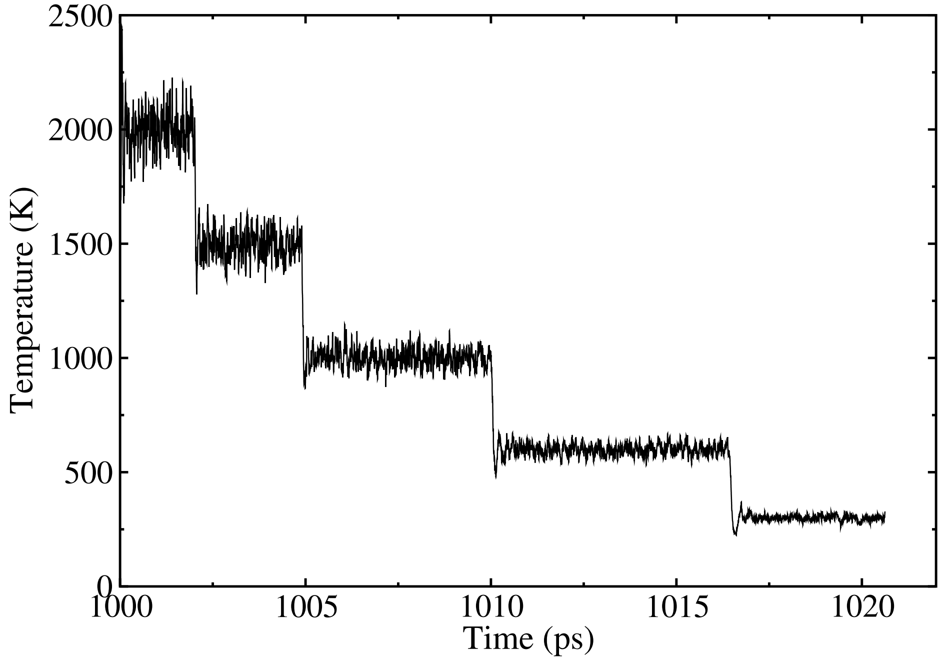

Figure S1: Thermal cycle followed by the *ab-initio* SiO_2 model.

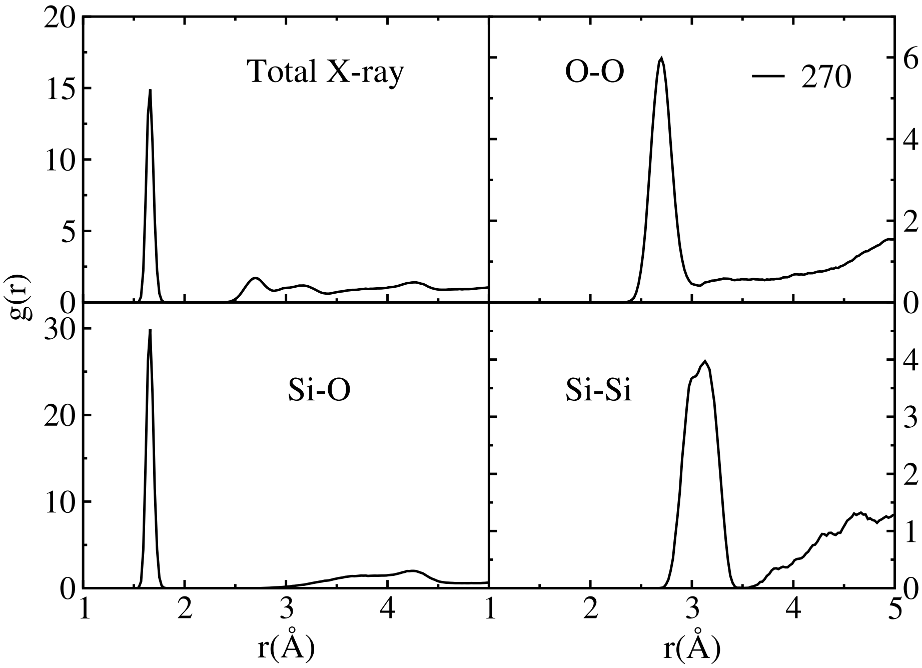

Figure S2: Comparison of total X-ray and partial O-O, Si-O, Si-Si g(r) PDFs for various simulation sizes.

Te and O weights to the displacement at a given normal mode

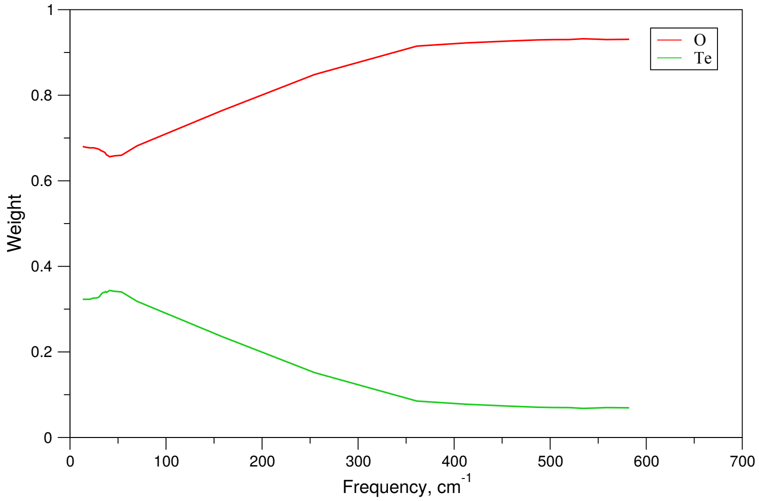

Figure S3: Frequency dependence of displacement weights of Te and O atoms in Raman active vibrational modes.

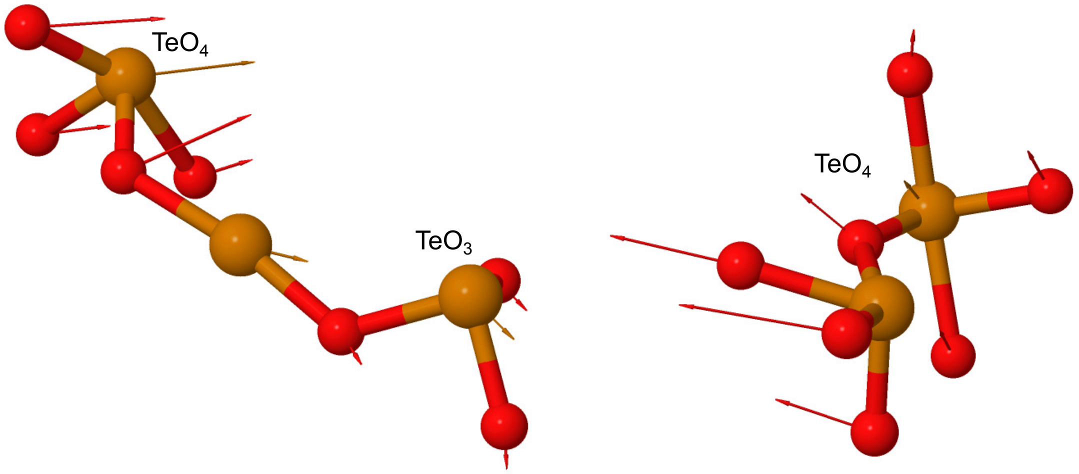

Figure S4: Atomic displacements pattern of an amorphous TeO_2 fragment. In left part one TeO_4 structural unit displaced with respect to TeO_3 structural unit, moving in perpendicular direction. In right part competitive displacements of two TeO_4 structural units is shown (the top unit shifts up, the other one shifts left).

VDOS of crystalline oxides

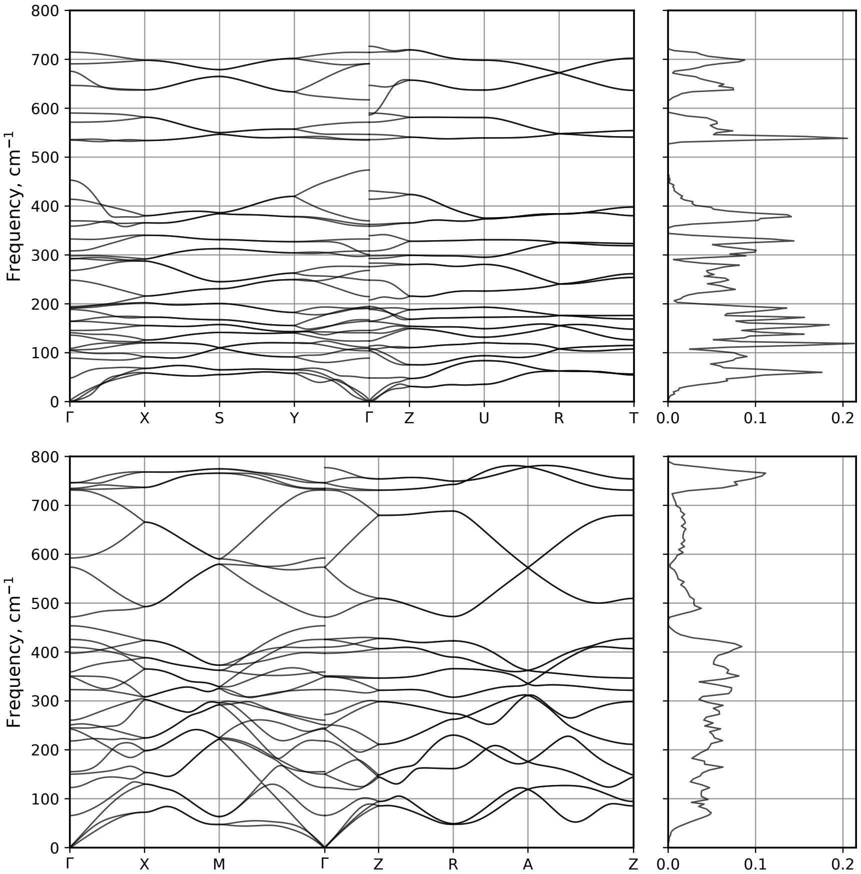

Figure S5: Phonon dispersion branches and vibratrional density of states of γ-TeO$_2$ (top) and crystobalite α-SiO$_2$ (bottom) calculated using supercell approach. The dynamical matrix was calculated for 4×4×3 supercell using finite difference method. The density of vibrational states (VDOS) is calculated as formally defined by equation: $g(\omega) = \frac{1}{N}\sum_{\nu,q}\delta(\omega - \omega_\nu(\mathbf{q}))$, where N is the number of unit cells, ν is the band index and $\mathbf{q}$ is the q-point. The Dirac delta function $\delta(x)$ is substituted by Gaussian function with constant standard deviation.

Boson peak frequency and cation-cation distances

Table S1: Boson peak frequency of common oxides.

Compound	Frequency, cm^{-1}		
TeO_2	34^a	75^b	35^c
SiO_2	65^a	50^d	
B_2O_3	30^e		
GeO_2	40.5^f		

[a] This work
[b] Ref. 6 (Lowest frequency peak in vibrational density of states).
[c] Ref. 7
[d] Ref. 8
[e] Ref. 9
[f] Ref. 10

Table S2: The most probable nearest neighbor distances in glassy TeO_2 and glassy SiO_2.

Property	distance value, Å	
	TeO_2	
d(Te-Te)	3.75^a	3.7^b
d(Te-O)	1.96^a	1.9^b
d(O-O)	2.79^a	2.9^b
	SiO_2	
d(Si-Si)	3.1^c	3.2^d
d(Si-O)	1.6^c	1.6^d
d(O-O)	2.6^c	2.5^d

[a] Ref. 11
[b] Ref. 6
[c] This work
[d] Ref. 12

Appendix 1: Finite differences method

According to Ref.[13] the Raman tensor of vibrational mode is defined as derivative of linear dielectric susceptibility χ with respect to normal mode ξ:

$$A_{ij} = \frac{d\chi_{ij}}{d\xi} = \sum_{\alpha,\beta} \frac{\partial \chi_{ij}}{\partial \tau_{\alpha\beta}} u_{\alpha\beta}, \tag{1}$$

where $u_{\alpha\beta} = \frac{\partial \tau_{\alpha\beta}}{\partial \xi}$ is a vector of atomic displacement of α'th atom along β Cartesian direction.

The calculation of derivative in equation (1) by finite difference method can be implemented in two general approaches. The first one corresponds to the distortion of relaxed structure according to normal modes, i.e. for each Raman active vibrational mode atomic positions are shifted by vector of atomic displacements ξ_m with respect to equilibrium atomic positions r_0 in positive and negative direction, then for each disturbed structure the susceptibility tensor is calculated. Then the derivative for each vibrational mode is calculated as follows:

$$\frac{d\chi_{ij}}{d\xi} = \frac{\chi(r_0 + \xi_m) - \chi(r_0 - \xi_m)}{2|\xi_m|} \tag{2}$$

The second approach is devoted to calculations of derivatives with respect to atom α displacements along Cartesian directions τ_β by finite difference method followed by multiplication on vector $u_{\alpha\beta}$ (right part of equation (1)).

The choice of the method depends on symmetry of the structure under study.

References

(1) VandeVondele, J.; Krack, M.; Mohamed, F.; Parrinello, M.; Chassaing, T.; Hutter, J. Quickstep: Fast and accurate density functional calculations using a mixed Gaussian and plane waves approach. *Comput. Phys. Commun.* **2005**, *167*, 103–128.

(2) Perdew, J. P.; Burke, K.; Ernzerhof, M. Generalized gradient approximation made simple. *Phys. Rev. Lett* **1996**, *77*, 3865.

(3) VandeVondele, J.; Hutter, J. Gaussian basis sets for accurate calculations on molecular systems in gas and condensed phases. *J. Chem. Phys.* **2007**, *127*, 114105.

(4) Goedecker, S.; Teter, M.; Hutter, J. Separable dual-space Gaussian pseudopotentials. *Phys. Rev. B* **1996**, *54*, 1703.

(5) Carré , A.; Berthier, L.; Horbach, J.; Ispas, S.; Kob, W. Amorphous silica modeled with truncated and screened Coulomb interactions: A molecular dynamics simulation study. *The Journal of Chemical Physics* **2007**, *127*, 114512.

(6) Pietrucci, F.; Caravati, S.; Bernasconi, M. TeO_2 glass properties from first principles. *Phys. Rev. B* **2008**, *78*, 064203.

(7) Zaki, M. R.; Hamani, D.; Dutreilh-Colas, M.; Duclre, J.-R.; Masson, O.; Thomas, P. Synthesis, thermal, structural and linear optical properties of new glasses within the TeO2-TiO2-WO3 system. *J. Non-Cryst. Solids* **2018**, *484*, 139–148.

(8) Malinovsky, V.; Novikov, V.; Surovtsev, N.; Shebanin, A. Investigation of amorphous states of SiO2 by Raman scattering spectroscopy. *Physics of the solid state* **2000**, *42*, 65–71.

(9) Hassan, A.; Börjesson, L.; Torell, L. The boson peak in glass formers of increasing fragility. *Journal of Non-Crystalline Solids* **1994**, *172-174*, 154–160.

(10) Rossi, F.; Baldi, G.; Caponi, S.; Maschio, R. D.; Fontana, A.; Orsingher, L.; Zanatta, M. The vibrational dynamics of GeO2 at the glass transition: a Raman and Brillouin scattering study. *Philosophical Magazine* **2011**, *91*, 1910–1916.

(11) Raghvender, R.; Bouzid, A.; Cadars, S.; Hamani, D.; Thomas, P.; Masson, O. Structure of amorphous TeO 2 revisited: A hybrid functional ab initio molecular dynamics study. *Phys. Rev. B* **2022**, *106*, 174201.

(12) Soules, T. F. A molecular dynamic calculation of the structure of sodium silicate glasses. *The Journal of Chemical Physics* **1979**, *71*, 4570–4578.

(13) Cardona, M., G.Gntherodt,, Eds. *Light scattering in solids II*; Springer-Verlag: Berlin, 1982.